Monthly Notices of the ROYAL ASTRONOMICAL SOCIETY
MNRAS **00,** 1 (2023) https://doi.org/10.1093/mnras/stad1270

Witnessing the intracluster medium assembly at the cosmic noon in JKCS 041

S. Andreon [1]★ C. Romero,[2,3,4] H. Aussel,[5] T. Bhandarkar,[4] M. Devlin,[4] S. Dicker [4] B. Ladjelate,[6] I. Lowe,[7,4] B. Mason [8] T. Mroczkowski [9] A. Raichoor [10] C. Sarazin[11] and G. Trinchieri[1]

[1]*INAF–Osservatorio Astronomico di Brera, via Brera 28, I-20121, Milano, Italy*
[2]*Center for Astrophysics | Harvard & Smithsonian, 60 Garden Street, Cambridge, MA 02138, USA*
[3]*Green Bank Observatory, 155 Observatory Road, Green Bank, WV 24944, USA*
[4]*Department of Physics and Astronomy, University of Pennsylvania, 209 South 33rd Street, Philadelphia, PA 19104, USA*
[5]*AIM, CEA, CNRS, Université Paris-Saclay, Université Paris Diderot, Sorbonne Paris Cité, F-91191 Gif-sur-Yvette, France*
[6]*Instituto de Radioastronomia Milimetrica (IRAM), Granada, Spain*
[7]*Department of Astronomy, University of Arizona, Tucson, AZ 85721, USA*
[8]*National Radio Astronomy Observatory, 520 Edgemont Road, Charlottesville, VA 22903, USA*
[9]*European Southern Observatory, Karl-Schwarzshild-Str. 2, D-85748 Garching b. München, Germany*
[10]*Lawrence Berkeley National Laboratory, 1 Cyclotron Road, Berkeley, CA 94720, USA*
[11]*Department of Astronomy, University of Virginia, P.O. Box 400325, Charlottesville, VA 22904, USA*

Accepted 2023 April 19. Received 2023 April 17; in original form 2023 January 4

ABSTRACT

In this work, we study the intracluster medium (ICM) of a galaxy cluster at the cosmic noon: JKCS 041 at $z = 1.803$. A 28 h long Sunyaev-Zel'dovich (SZ) observation using MUSTANG-2 allows us to detect JKCS 041, even if intrinsically extremely faint compared to other SZ-detected clusters. We found that the SZ peak is offset from the X-ray centre by about 220 kpc in the direction of the brightest cluster galaxy, which we interpret as due to the cluster being observed just after the first passage of a major merger. JKCS 041 has a low central pressure and a low Compton Y compared to local clusters selected by their ICM, likely because the cluster is still in the process of assembly but also in part because of a hard-to-quantify bias in current local ICM-selected samples. JKCS 041 has a 0.5 dex fainter Y signal than another less massive $z \sim 1.8$ cluster, exemplifying how much different weak-lensing mass and SZ mass can be at high redshift. The observations we present provide us with the measurement of the most distant resolved pressure profile of a galaxy cluster. Comparison with a library of plausibly descendants shows that JKCS 041 pressure profile will likely increase by about 0.7 dex in the next 10 Gyr at all radii.

Key words: galaxies: clusters: general – Galaxies: clusters: individual: JKCS 041 – Galaxies: clusters: intracluster medium – X-rays: galaxies: clusters.

1 INTRODUCTION

The redshift around two is a key epoch for galaxies and clusters: The cosmic star formation rate and the black hole growth peak at about this redshift (Madau & Dickinson 2014) and the first massive clusters emerge from the cosmic web (Arnaud et al. 2009). At this epoch of high star formation rates, active galactic nucleus (AGN) and merger activity, the intracluster medium (ICM) is heavily shaped by accretion shocks, heating from stellar winds associated with star formation of member galaxies, and mechanical heating and turbulence generated by AGNs (McNamara et al. 2005). A characterization of the ICM of clusters at this epoch would therefore offer a measurement of the efficiency of these feedback mechanisms and of the gas circulation in these initial stages of the cluster formation. However, in spite of extensive searches, in the last 10 yr we were unable to characterize the ICM of any cluster at $z > 2$, the most distant characterized clusters being XLSSC122 (Willis et al. 2020) at $z = 1.98$, JKCS 041 (Andreon et al. 2009, 2014; Newman et al. 2014) at $z = 1.803$ and IDCS J1426.5+3508 (Stanford et al. 2012; Andreon et al. 2021) at $z = 1.75$. At $z > 2$, ICM detections are still quite uncertain; the ICM detection of a $z = 2.5$ cluster by Wang et al. (2016) has been questioned by Champagne et al. (2021). The $z = 2.16$ Spiderweb structure is dominated by the wings of point spread function (PSF) of the central bright AGN and by inverse-Compton scattering on the jet emission (Tozzi et al. 2022). The latter components outshine the tentative ICM detection at energies larger than about 1 keV (Tozzi et al. 2022), while the available Chandra data below 0.8 keV are noisy at best because of the contaminant on the optical blocking filter. The complexity of this handful of arcsec wide sky region, with two bright AGNs, two bright jets, and at best a very weak ICM emission, has been pointed out by the SZ analysis of Di Mascolo et al. (2023). The properties of the ICM at this key epoch are therefore poorly known because of the difficulty of acquiring spatially resolved data adequate for the purpose. XLSSC122 and JKCS 041 have X-ray radial surface brightness profiles (Andreon et al. 2009; Mantz et al.

★ E-mail: stefano.andreon@inaf.it

2018). IDCS J1426.5+3508 instead, thanks to spatially resolved Sunyaev-Zel'dovich (SZ) and X-ray data, has all its thermodynamic profiles determined. This allowed Andreon et al. (2021) to find a sizeable gas, heat, and entropy transfer at $r > 300$ kpc in IDCS J1426.5+3508, while the cluster central region has likely reached the final stage. Of course, with just one example studied in detail, it is impossible to say whether the inside-out ICM assembly seen in IDCS J1426.5+3508 is a general feature of the whole cluster population at those redshifts. As mentioned, $z \sim 2$ is an epoch of intense merger activity. The ICM of several major mergers at low to intermediate redshifts have been studied in detail (e.g. Cl J0152−1357 and Bullet clusters, Massardi et al. 2010; Menanteau et al. 2012), but adequate data to investigate the ICM properties of one such object at $z \sim 2$ are still lacking. At this redshift, the fraction of disturbed clusters is expected to be high, making this investigation even more pressing.

In this paper, we report very deep SZ observations of JKCS 041 sufficient to measure the radial profile of the cluster pressure and therefore to study its ICM. JKCS 041 is an intermediate-mass cluster (a few 10^{14} $M_\odot$, Andreon et al. 2014) at $z = 1.803$ (Andreon et al. 2014; Newman et al. 2014) with hot gas detected by Chandra (Andreon et al. 2009). With 19 spectroscopic members, a well-defined red sequence, and an extensive multiwavelength coverage, this system is perhaps the most studied cluster in the high redshift Universe; e.g. it is the only cluster so far with measurements of velocity dispersion of their individual passive galaxies (Prichard et al. 2017). Mostly based on the dynamics of the cluster galaxies, JKCS 041 is suspected to have substructure and to be a merger in progress (Prichard et al. 2017). Unlike other clusters, JKCS 041 is not ICM-selected (was discovered as galaxy overdensity and later follow-up, Andreon et al. 2009) and therefore does not share the common bias of ICM-selected samples that have clusters with large signals overrepresented (and clusters with low signals underrepresented or absent), see e.g. Andreon et al. (2011).

Throughout this paper, we assume $\Omega_M = 0.3$, $\Omega_\Lambda = 0.7$, and $H_0 = 70$ km s^{-1} Mpc^{-1}. The results of stochastic computations are given in the form $x \pm y$, where x and y are the posterior mean and standard deviation. The latter also corresponds to 68 per cent uncertainties because we only summarize posteriors close to Gaussian in this way. All logarithms are in base 10.

2 OBSERVATIONS, DATA REDUCTION, AND ANALYSIS

2.1 Weak lensing

Kim et al. (2023) performed a weak lensing analysis of JKCS 041 based on WFC3 imaging data and photometric redshifts presented in Newman et al. (2014). The authors found a mass of $M_{200} = 4.7 \pm 1.5\,10^{14}\,M_\odot$. The analysis makes a two-dimensional fit using Navarro, Frenk & White (1997) profiles with the Diemer & Joyce (2019) mass-concentration relation. Two mass components were jointly fitted, the JKCS 041 cluster itself and a spectroscopic confirmed $z = 1.13$ group about 1 arcmin south-west of the X-ray centre (the plus sign in Fig. 1, Newman et al. 2014).

A similar analysis for the other cluster often mentioned in this work, IDCS J1426.5+3508 at $z = 1.75$ returns a lower mass of $M_{200} = 2.2^{+1.1}_{-0.7}\,10^{14}\,M_\odot$ (Jee et al. 2017), in agreement with its lower richness (Andreon 2013). The M_{500} masses of these two clusters, used here, have been derived from M_{200} following Ragagnin et al. (2021).

2.2 Galaxy dynamics

Using the K-band multiobject spectrograph at VLT, Prichard et al. (2017) determined precise ($\lesssim 100$ km s^{-1}) redshifts of 16 JKCS 041 galaxies that were known to be members using *Hubble Space Telescope* redshifts (with $\sim$500 km s^{-1} precision) in Newman et al. (2014). These are shown in Fig. 1 as squares colour-coded by relative velocity. The spatial distribution of the relative velocities (note that the red squares are all in the cluster South) suggest that JKCS 041 is composed by two merging sub-clusters (Prichard et al. 2017).

2.3 X-ray

JKCS 041 was observed with *Chandra* ACIS-S for 75 ks; data reduction and analysis are described in Andreon et al. (2009). Here we use the same data to derive an image to be used as a comparison to the SZ image.

To optimize the imaging of the cluster, we start from Scharf (2002), who discusses the optimal energy range to be used to image galaxy clusters at $z < 1$ with maximal signal to noise when photons cannot be weighted but can only be taken or discarded depending on their energy. We improve upon his work eliminating the redshift limit and weighting photons with a weight given by the information content of each (infinitesimal) energy bin. The weight is computed as the ratio between the cluster and the background spectra. The cluster is modelled with an APEC spectrum with the temperature measured for JKCS 041 (from Andreon et al. 2009) and its redshift (from Newman et al. 2014) to enforce regularity. The background is measured from the photons falling in the same chip but outside the cluster solid angle. Compared with the common [0.5, 2] keV choice, the optimal weight resemble a Maxwell distribution, with a peak at about 1 keV, a full width at half-maximum (FWHM) of 0.9 keV, and a tail higher energies. The decrease at $\sim$1.7 keV is due to the presence of a background line there (as already remarked by Scharf 2002), while the decrease at lower energies is due to the increased background. After weighing and getting rid of point sources (interpolating over the tiny regions occupied by them), we apply an adaptive filter to the data using CIAO csmooth (based on Ebeling et al. 2006) to keep only features with $S/N > 3$, as already done in Andreon et al. (2009). Isocontours of the image so obtained are shown in Fig. 1.

2.4 SZ data

JKCS 041 was observed for 28 h (overhead included) with MUSTANG-2 between 2018 December and 2021 January. MUSTANG-2 is a 215-element array of feedhorn-coupled TES bolometers (Dicker et al. 2014) at the 100m Green Bank telescope (GBT) working at 90 GHz. When mounted on the GBT, MUSTANG-2 has about 10 arcsec FWHM resolution and an instantaneous field of view of 4.5 arcmin.

JKCS 041 was observed with Lissajous daisy scans, typically with a 2.5 arcmin radius. The data were calibrated using preferentially Solar systems objects, and also ALMA calibrators (Fomalont et al. 2014; van Kempen et al. 2014). Our SZ maps are calibrated to Rayleigh–Jeans brightness temperature (K_{RJ}), adopted throughout this paper. The final map has an RMS noise of 23 μK when smoothed to the beam resolution, within the central 2 arcmin radius. A beam profile specific to this cluster observations is created by stacking all secondary (point-source) calibrators interspersed during these observations (see Ginsburg et al. 2020). The beam FWHM of the final map is 9.5 arcsec.

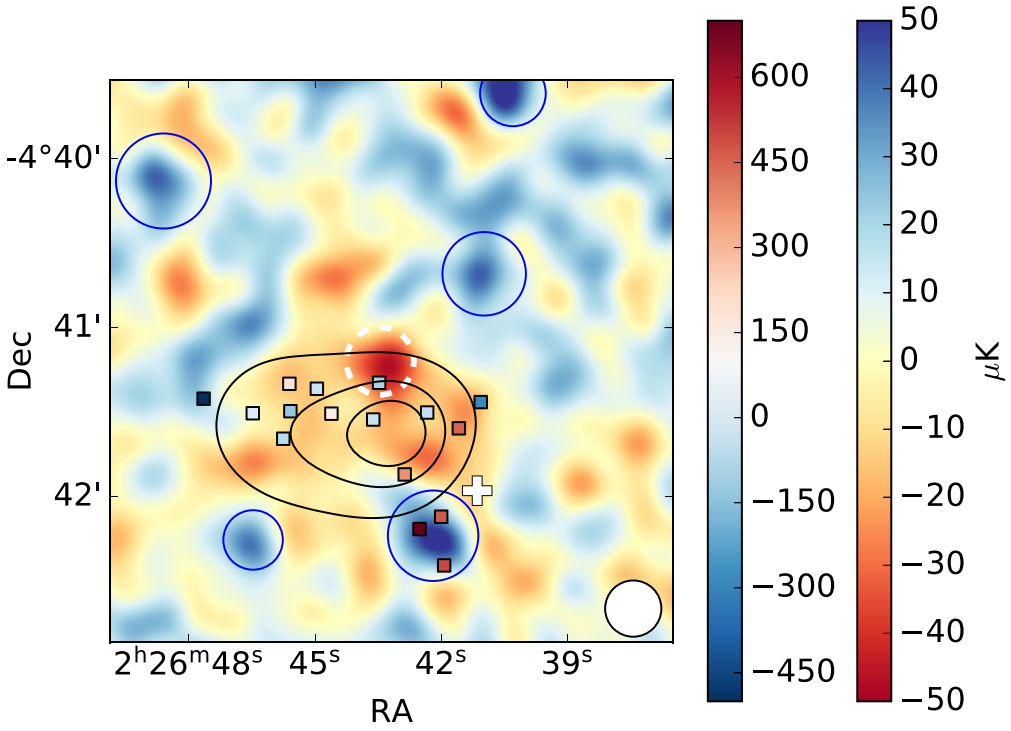

Figure 1. Multiwavelength view of JKCS 041. The image is the MUSTANG-2 SZ map smoothed with a Gaussian with $\sigma = 6$ arcsec. Large blue circles indicate the regions flagged in our analysis because of the presence of point sources. The MUSTANG-2 beam is indicated in the bottom right. The SZ peak is indicated by a dashed white circle of 12 arcsec radius and the centre of a $z = 1.13$ group is indicated by a plus sign. Black contours are X-ray isocontours of the adaptively smoothed, optimally extracted Chandra image. Spectroscopic confirmed cluster members are indicated by squares colour-coded by relative velocity (inner colour bar, in km s^{-1}). The SZ and X-ray peaks are offset by about 26 arcsec, in a nearly North–South direction. Galaxies in the South have high positive velocities. The cluster brightest cluster galaxy is the square inside the white dashed circle.

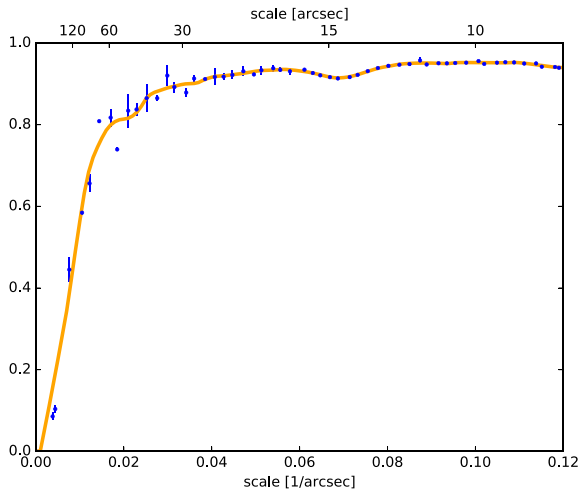

Figure 2. JKCS 041 MUSTANG-2 transfer function. Signal at scales smaller than 1 arcmin is, by and large, preserved by the MIDAS data reduction but is increasingly reduced with increasing scales.

The data were reduced following the traditional approach (named MIDAS in Romero et al. 2020, to which we refer for details): time ordered data from unresponsive detectors or from bad scans and glitches are flagged, remaining ones are filtered to subtract atmospheric and electronic background. This filtering also removes some (cluster) signal, which needs to be accounted for during the analysis using the transfer function, shown in Fig. 2. The transfer function is larger than 0.8 at scales smaller than 1 arcmin, then drops to lower values. Since atmospheric conditions were less stable during the observations of JKCS 041 than of IDCS J1426.5+3508, a more aggressive filtering was needed for JKCS 041 data. This resulted in a transfer function that drops to low values at smaller scales (compared to the one of IDCS J1426.5+3508, shown in Andreon et al. 2021).

The resulting map is shown in the left-hand panel of Fig. 1. The SZ peak is at (RA, Dec) = (2:26:43.2, −4:41:13). A few point sources are visible (dark blue in the figure surrounded by blue circles) and pixels contaminated by them are flagged and ignored during further cluster analysis.

For completeness, we report that JKCS 041 was also observed for 17 h with the NIKA2 camera (Adam et al. 2018) at 150 and 250 GHz at the IRAM 30m telescope. The cluster SZ signal is not obvious in the preliminary reduction of this shorter exposure taken with a smaller telescope, although there is a (negative) blip in the NIKA2 150 GHz map at the location of the MUSTANG-2 (negative) peak. We defer a full analysis of the properly reduced NIKA2 data to a later paper.

2.5 The SZ-X offset

The X-ray peak is at (RA, Dec) = (2:26:43.1, −4:41:36), about 26 arcsec (about 220 kpc) South of the SZ one derived in Section 2.4 A spatial offset between the X-ray and SZ centres is possible because of the different dependence of these two observables on electron density and temperature. This has already been seen e.g. in the merging clusters Cl J0152-1357 (Massardi et al. 2010) and Bullet (Menanteau et al. 2012). According to hydrodynamic simulations in Zhang et al.

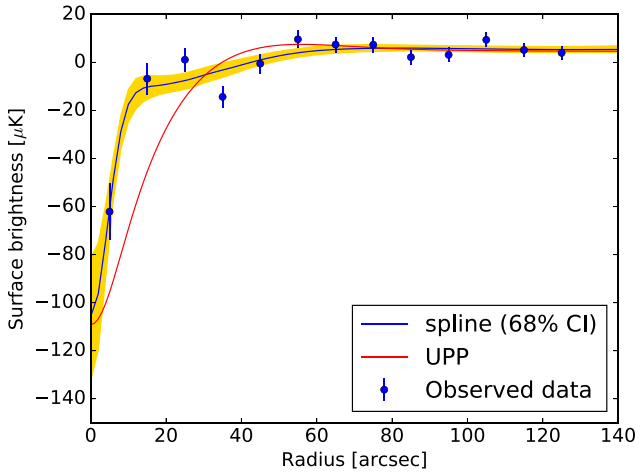

Figure 3. JKCS 041 SZ surface brightness profile (points with error bars) and 68 per cent uncertainties on the fitted model. The adopted spline for the pressure profile is able to well describe the observed data, whereas a universal pressure profile (UPP) with parameters fixed to Arnaud et al. (2010, red curve) does not.

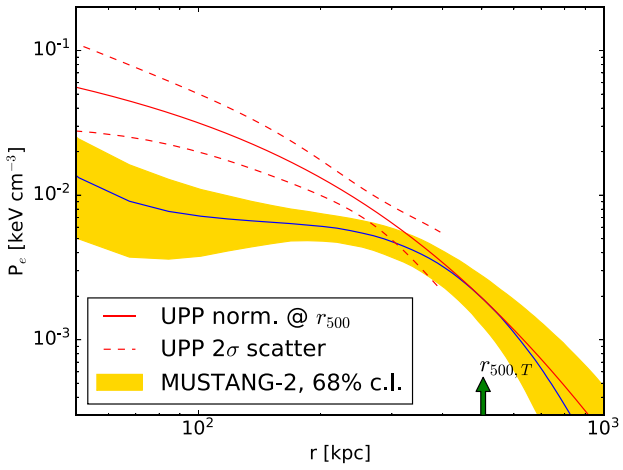

Figure 4. Observed MUSTANG-2 JKCS 041 electron pressure profile with 68 per cent uncertainties (solid curve and shading) versus a universal pressure profile (UPP) with same pressure at r_{500}. Note that the displayed radial range includes radii poorly sampled by MUSTANG-2 ($r \gtrsim 1$ arcmin, about 500 kpc at the cluster redshift). The Arnaud et al. (2010) scatter around the universal pressure profile is also indicated.

(2014), large offsets are produced just after the pericentric passage during near head-on major mergers of clusters with $M > 10^{14}\,M_\odot$. Therefore, we interpret the SZ-X offset as due to the cluster being observed just after a major merger, as a part of the emergence of the first massive clusters from the cosmic web at early times. The spatial SZ-X offset corroborates the suggestion by Prichard et al. (2017) that JKCS 041 still shows traces in the galaxy dynamics of the two sub-clusters that formed it; see Fig. 1 with large positive velocities (red) points regrouped in the cluster south. In JKCS 041, the SZ-X offset is in the North–South direction, as the two groups identified by Prichard et al. (2017; the red points).

Judging from Zhang et al. (2014) simulations, the main cluster is coincident with the SZ peak while the colliding cluster is South of it and came from North with $\Delta v \approx 500$ km s^{-1} and is seen ≈0.5 Gyr after the pericentric after a nearly head-on collision. This would produce an X-ray peak about 250 kpc South of the SZ peak, as observed in JKCS 041. In the simulations, the two sub-clusters have a mass of 1–2 10^{14} $M_\odot$ (that are cluster masses at $z = 1.8$) and their summed mass is consistent with the observed JKCS 041 weak lensing mass. Tailored (and more precise) constraints on the JKCS 041 colliding sub-clusters (e.g. gas fraction) and merger parameters (e.g. relative velocity and projection effects) accounting for the observational setup (e.g. SZ transfer function) and constrained by measured quantities (mass, Compton-Y, etc.) are presented in Felix et al. (2023).

2.6 The depressed pressure profile

Fig. 3 shows the cluster SZ radial surface brightness profile, extracted with 10 arcsec radial annuli centred on the SZ peak after flagging the point sources indicated in Fig. 1. The cluster is quite faint, with a peak of ∼ 60 μK. The brightness profile levels off to ≈ 5 μK, a non-zero level (that we name pedestal) induced by the data reduction that forces the map to have zero mean.

The three-dimensional pressure profile is derived fitting the SZ data with a modified version of `PreProFit` (Castagna & Andreon 2019), accounting for the transfer function, PSF (beam), and pedestal level, following Andreon et al. (2021). The conversion from K to Compton y is derived in Andreon et al. (2021) and, since it is (minimally) T-dependent we adopt the observed temperature $kT = 7.6$ keV (Andreon et al. 2009).

Following Andreon et al. (2021), we adopt a pressure profile given by a cubic spline in log-log space with knots at radii of $r = 5$, 15, 30, and 60 arcsec. By adopting a cubic spline we allow the shape of the pressure profile to vary almost arbitrarily while keeping it continuous and doubly differentiable. By defining the spline in log quantities (log pressure versus log radius), we naturally exclude non-physical (negative) values of pressure and radius and we can approximate a large variety of profiles, and their derivatives, including the commonly parametrized pressure profile as in Nagai et al. (2007). Our model then has five variables: the pressures at the four radii, P_0, P_1, P_2, and P_3, and the pedestal value of the SZ surface brightness. Our analysis assumes spherical symmetry, uniform priors, zeroed for unphysical values (e.g. pressure cannot be negative). In particular, since the total mass of the cluster is finite, the logarithmic slope of the pressure should be steeper than −4 at large radii (Romero et al. 2018). We therefore adopted a logarithmic slope <-2 at $r = 1$ Mpc as prior. This prior could alternatively be expressed as a maximal value for the pedestal level. The imposition of this prior is necessary primarily to distinguish a radially flat background from a radially flat cluster signal.

We find $P_i = 19 \pm 13$, 7 ± 3, 5 ± 1, 1.9 ± 0.7 eV cm^{-3}, and a pedestal level of 5 ± 1 μK with covariances illustrated in Fig. 5. We found a χ^2 of 17 for 8 degrees of freedom. There is a ∼2 per cent probability to observe a larger χ^2 assuming the model best fit. The two points at $r \sim 25$ and 35 arcsec carry the largest contributions to the total χ^2, with the outer radius corresponding to local (negative) maxima in the SZ signal at NE and SW in Fig. 1 likely induced by the cluster merger. Fig. 3 shows the best-fitting model on top of the observed data. Fig. 4 shows the pressure profile as a blue line with 68 per cent uncertainty as the shaded area. This is the most distant cluster with a resolved SZ-based pressure profile, at only marginally larger redshift than the previous record holder IDCS J1426.5+3508 (Andreon et al. 2021).

The JKCS 041 integrated spherical and cylindrical Componization parameter within r_{500} are $7.7 \pm 1.8\ 10^{-6}$ Mpc^2 and $10 \pm 1\ 10^{-6}$ Mpc^2, respectively. The JKCS 041 integrated cylindrical Componization

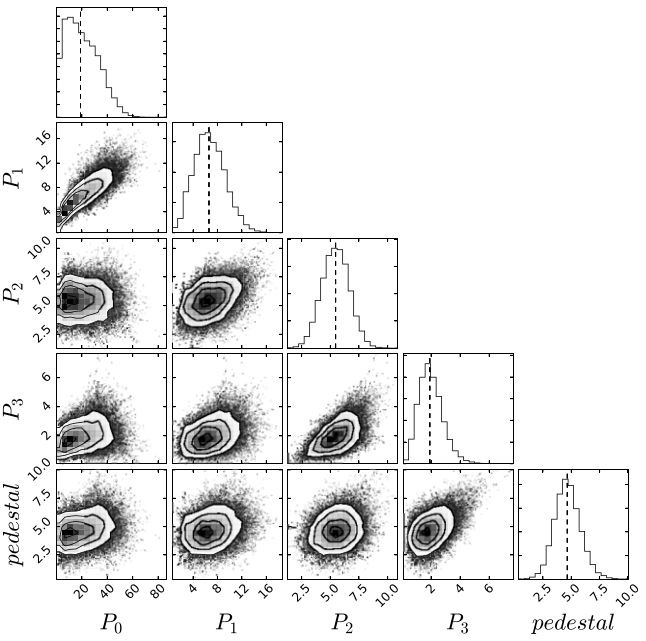

Figure 5. Joint and marginal probability contours for our SZ fit. Units: eV cm^{-3} for pressure parameters and μK for pedestal.

parameter within 30 arcsec is 4.1 10^{-6} Mpc^2, consistent with (below) the 95 per cent upper limit of 6.8 10^{-6} Mpc^2 reported in Culverhouse et al. (2010). The latter is based on an inward extrapolation of the (lack of) signal measured on larger scales assuming a radial profile for JKCS 041 close to the universal pressure profile, which however does not fit our data (Figs 3 and 4).

Fig. 4 shows that JKCS 041 pressure profile is centrally depressed compared to the universal pressure profile (UPP, Arnaud et al. 2010) being outside the 2σ UPP range at several radii (larger significance requires a larger comparison sample). In this comparison, we adopt Arnaud et al. (2010) best-fitting values, r_{500} as derived from the X-ray temperature in Andreon et al. (2014) and we fixed the normalization to have a match at r_{500}. How well (badly) this profile matches the observed data is shown in Fig. 3 (red line). The shapes of the profile do not match: JKCS 041 has a small-size central emission over a faint flat profile, unlike the universal pressure profile, that is spatially larger and slowly changing. Using the weak-lensing mass instead of the one estimated from temperature does not alter our conclusion. This is the third example of a cluster selected independently of the ICM content whose pressure profile turns out to be clearly depressed (with CL2015, Andreon et al. 2019 and IDCS J1426.5+3508, Andreon et al. 2021), confirming previous claims that were either indirect (Di Mascolo et al. 2019) or of lower significance (Dicker et al. 2020). However, JKCS 041 and IDCS J1426.5+3508 are manifestly observed during their ICM assembly, and perhaps for this reason their ICMs have not yet reached their final configuration, unlike CL2015.

We have investigated whether the observed deviations of the SZ emission from a circular symmetric universal pressure profile centred on the X-ray centre might be due to point sources. However, we find this unlikely because a universal pressure profile has an extent much wider than the MUSTANG-2 PSF. In fact, at least four sources would be required to match the extent, but: (i) we expect about 0.2 sources on average from number counts; (ii) there are no sources detected at 90 GHz; and (iii) there are no sources detected at 1.4 or 855 GHz, which instead would be expected for 90 GHz sources with a non-peculiar spectral energy distributions. In detail, only focusing to the inner 30 arcsec, we need at least four sources all with similar fluxes (70–100 μJy), appropriately spaced apart (about 17 arcsec from each other), and with almost unique spectral energy distributions in order not to be detected in the available VLA data at 1.4 GHz (Bondi et al. 2003) and in SPIRE 855 GHz data (Schulz et al. 2017). In particular, a 70 μJy source at 90 GHz would be detected at 1.4 GHz if its spectral slope is steeper than −0.2 and at 855 GHz if its spectral emission matches a grey body of 40 K (adopted to estimate the contamination in e.g. Sayers et al. 2013). This large density of ad hoc sources in a small solid angle (with p-value probability 5.7 10^{-5} based on the 0.2 sources observed on average in a 30 arcsec aperture by Zavala et al. 2021) and the required characteristics would still not be able to mimic the profile at larger scales nor to make the SZ emission circularly symmetric and co-centred with the X-ray. For the sake of completeness, we also consider the case in which the matching to flux and extent of the universal pressure profile is achieved by contamination by many faint sources. To explore this case, we randomly draw distributions of fluxes from the Zavala et al. (2021) number counts (extrapolated down to 10 μJy) within a solid angle with 30 arcsec radius and we count how many times we obtain a total net flux larger than 320 μJy (to match the missing flux of the universal pressure profile within the considered solid angle) with individual fluxes in the simulated cluster aperture fainter than 70 μJy (to avoid to be detected at 1.4, 90, or 855 GHz). This very rarely happens in our simulations, about twice every 10^5 times. This computation neglects the fact that we need a peculiar spatial distribution of sources: a higher flux at the centre of the aperture (where the SZ signal should be made larger) and an appropriate azimuthal flux distribution to achieve a spherically symmetric profile centred on the X-ray centre starting from an observed SZ distribution with a peak 26 arcsec away from it. This configuration is highly unlikely. To summarize, we could not find a reasonable configuration of points sources that could explain the observed mismatch between the X-ray and SZ centres, the asymmetric SZ emission, and the excess at 35 arcsec, given the much larger extent of the cluster emission compared to the PSF. We therefore conclude that point sources are extremely unlikely to alter our results.

3 PLAUSIBLE EVOLUTION

Fig. 6 compares the JKCS 041 pressure profile (blue solid line) to a library of profiles derived for clusters in the nearby Universe (corridors). The red dotted corridor indicates the $\pm 2\sigma$ range as derived by X-COP (Ghirardini et al. 2019) for clusters with JKCS 041 M_{500} mass. Similarly to Fig. 4, JKCS 041 has a low pressure for its mass in the inner 200 kpc. This comparison, at fixed mass, is in our opinion misleading to study evolution: the mass of JKCS 041 cannot stay constant for about 10 Gy, not even if the cluster acquires zero mass, because the integration radius, corresponding to the overdensity Δ, becomes larger at low redshift as a result of the decrease of the mean density of the Universe (see Andreon et al. 2021 for discussion). To study evolution it is preferable to compare ancestors and descendants (Andreon & Ettori 1999). By selecting the 22 most massive clusters in the closest snapshot ($z = 1.71$) and their $z = 0$ descendants in the Magneticum simulation (Hirschmann et al. 2014; Dolag et al. 2016; Ragagnin et al. 2017), we find that by $z = 0$ the mass of JKCS 041 will plausibly have grown by 0.60 ± 0.16 dex. This computation actually uses clusters of slightly less mass than JKCS 041 ($0.64 < M_{500}/\mathrm{M}_\odot < 1.4$ versus 2.2 10^{14}) because of the limited volume of the simulation. The comparison of JKCS 041 to its descendants is shown by the green dashed corridor, marked by the $\pm 2\sigma$ range. This, wider, corridor also accounts for the uncertainty on

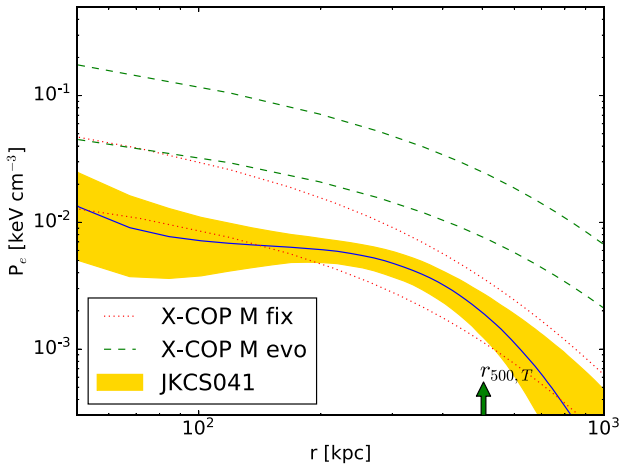

Figure 6. JKCS 041 pressure profile (mean value and 68 per cent uncertainties, blue line, and yellow shading) is compared to present-day clusters with the same M_{500} (the red dotted lines mark the 2σ range) and to its present-day expect descendants (the dashed green lines mark the 2σ range inclusive of the uncertainty on the mass accretion history). Compared to its present-day descendant, the pressure is low at all radii. To become a present-day cluster, the pressure must increase by 0.7 dex. Observed values at $r > 500$ kpc (about 1 arcmin) are very uncertain because these scales are heavily filtered.

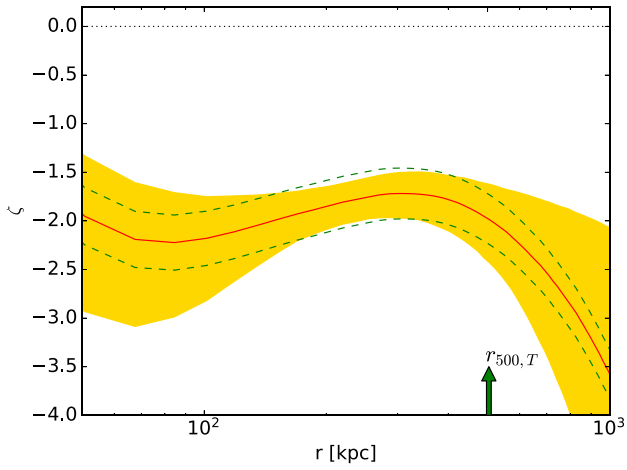

Figure 7. Pressure evolutionary rate ζ versus r (equation 1). The redshift evolution function $\zeta(r)$ of the JKCS 041 pressure profile (mean value and 68 per cent uncertainties, red line and yellow shading) is shown when compared to its present-day expected descendants. The dashed corridor marks twice the X-COP scatter about the average and accounts for the uncertain mass accretion history. Negative values indicate a lower pressure in the past, while the no-evolutionary case corresponds to $\zeta = 0$. The plot quantifies the evolutionary rate already visible in Fig. 6. The observed rate at $r > 500$ kpc is very uncertain because it is derived from data heavily filtered on these scales.

the mass growth. Compared to the library of possible descendants, the JKCS 041 pressure profile is low at all radii by about 0.7 dex.

To quantify the amount of evolution, following Andreon et al. (2021) we compute the evolutionary rate ζ, which is the exponent of E_z in:

$$P(r, z, M_z) = P(r, z = 0, M_{z=0}) E_z^{\zeta} \quad (1)$$

where $E_z = H(z)/H_0$ and $M_{z=0}$ is the $z = 0$ mass of the plausible descendant of the cluster with mass M_z at redshift z. Unlike other authors, we compare same radii in kpc, not radii scaled by r_{500} because the cluster content does not expand with the Universe (see Andreon et al. 2021 for details). As local, comparison, sample, we use the pressure profile derived from the X-COP sample (Ghirardini et al. 2019). Fig. 7 shows the derived evolutionary rate and quantifies what is already visible in Fig. 6: pressure is lacking at high z and must increase with a rate $\zeta \approx -2$ at most radii. The figure shows the uncertainty due to measurement errors (yellow shading) and that from the combination of the one coming from the variety of profiles at a fixed mass at $z = 0$ and of the scatter in accretion histories (dashed green corridor, marking the $\pm 2\sigma$ range). The large pressure change implied in this comparison indicates that JKCS 041 is in a very active phase, as also shown by the SZ-X offset. Unlike IDCS J1426.5+3508, the inner 200 kpc display a large evolutionary rate ζ, indicating that even the central part of JKCS 041 is far from the likely final status, in agreement with the SZ-X offset.

One caveat applies: the $z = 0$ clusters that we use as a local sample are ICM selected, either in X-ray (Fig. 4) or in SZ (Fig 6), whereas JKCS 041 is selected independently of its ICM content because it was discovered in near-infrared (and then followed up with Chandra and MUSTANG-2). ICM-selected clusters have, by selection, pressure profiles biased high and with reduced scatter because clusters with low pressure are underrepresented, or absent, in those samples (Andreon 2016; Andreon et al. 2019). A cluster with the JKCS 041 Compton parameter Y_{SZ}, or central Compton parameter $\tilde{y}_0$, is undetectable in the ACT (Hilton et al. 2021) or SPT (Bocquet et al. 2019) as discussed in Section 3.1, and also with Planck (Planck collaboration 2016) when $z \gtrsim 0.02$. Therefore, if sizeable samples of clusters with depressed profiles exist in the nearby Universe, the range seen in REXCESS or X-COP is reduced and biased, and our estimate of evolution biased high. We have demonstrated that at least one such cluster exists, CL2015 (Andreon et al. 2019). The same caveat applies to estimates of evolution by other authors (e.g. Pratt et al. 2022) that furthermore mix evolution with pseudo-evolution by scaling radii (see Andreon et al. 2021 for details and comments on earlier estimates).

The observed $\zeta \approx -1.5$ evolutionary rate is similar to values seen in the 22 clusters in the Magneticum simulation at $r > 200$ kpc but smaller at smaller radii (rates for individual simulated clusters are shown in Andreon et al. 2021 Fig. 16). In particular, in simulations inner radii are already pressured (i.e. $\zeta \approx 0$) and, if any, are overpressured at high z (i.e. $\zeta > 0$) compared to present-day descendants. On the other hand, a similar profile might be missing in the simulation simply because we have only 22 simulated clusters (of slightly lower mass) and major head-on mergers of massive subclusters, as JKCS 041 is, are rare (also in samples of 100, Wik et al. 2008).

3.1 The faintness of JKCS 041

Compared to other clusters with SZ observations, JKCS 041 is extremely faint, as illustrated in Fig. 8 comparing its central central Compton value $\tilde{y}_0$ and literature values. ACT values (small points) are from Hilton et al. (2021), while the JKCS 041 (red circle) and IDCS J1426.5+3508 (cyan square) $\tilde{y}_0$ values are derived using MUSTANG-2 data following the ACT definition (Hilton et al. 2021): we took the central value of the y map, derived by Abel (line of sight) projection of the pressure profile, and filtered with the convolution of a universal pressure profile with scale 2.4 arcmin and the ACT beam. For IDCS J1426.5+3508 we used MUSTANG-2 data in Andreon et al. (2021). We found $\tilde{y}_0 = 2.0 \times 10^{-5}$ and 6.6×10^{-5} for JKCS 041 and IDCS J1426.5+3508, respectively.

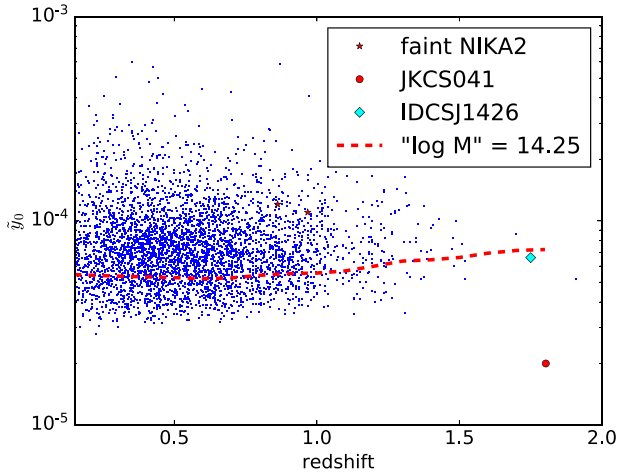

Figure 8. Central comptonization parameter $\tilde{y}_0$ of various samples. ACT clusters in Hilton et al. (2021) are indicated with small points, JKCS 041 and IDCS J1426.5+3508 are marked with a red circle and cyan diamond, respectively, whereas two clusters denoted as very weak in the paper presenting their SZ signal are identified by stars at $z \sim 0.9$. JKCS 041 is fainter by a factor of a few than these clusters. The $\log M_{500} = 14.25$ $M_\odot$ line is indicated, corresponding to the 10 per cent ACT completeness. This plot is the common mass-redshift plot except that here we use the observable $\tilde{y}_0$ instead of identifying it with mass. Using mass produces a slight vertical shift of each point such that the red dashed line becomes straight and flat.

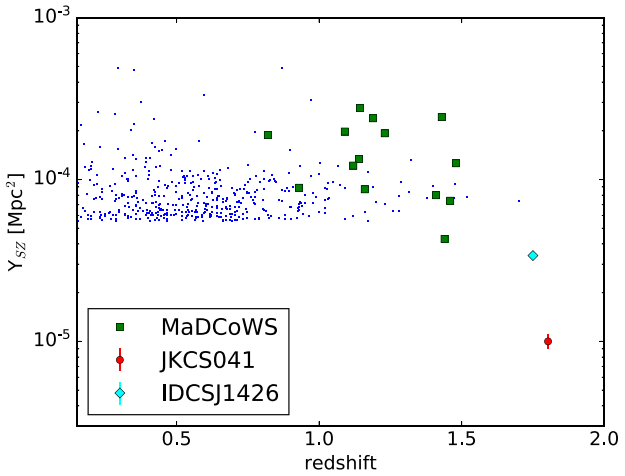

Figure 9. Cylindrical integrated Compton parameter Y_{SZ} within r_{500} for SPT clusters in Bocquet et al. (2020, small points), JKCS 041 (red circle), IDCS J1426.5+3508 (cyan diamond), and MaDCoWS clusters (squares). JKCS 041 is fainter by a factor of a few than the faintest SPT and MaDCoWS clusters. This plot is the common mass-redshift plot except that here we use the observable Y_{SZ} instead of identifying it with mass.

JKCS 041 is ∼4 times fainter than the 10 per cent ACT completeness value, indicated by a dashed line. As a way of comparison, a couple of clusters, denoted as very faint in the papers presenting them (Kéruzoré et al. 2020; Ricci et al. 2020), are indicated by stars (at $z \sim 0.9$) and they are almost 10 times brighter than JKCS 041. Fig. 9 repeats the comparison using SPT clusters from Bocquet et al. (2019) and Massive and Distant Clusters of WISE Survey (MaDCoWS) with a $\geq 5\sigma$ SZ detection from Dicker et al. (2020). The faintest of these clusters are brighter by a factor of a few compared to JKCS 041. JKCS 041 is a really faint cluster and indeed its surface brightness profile is noisier than that of IDCS J1426.5+3508 in spite of a much

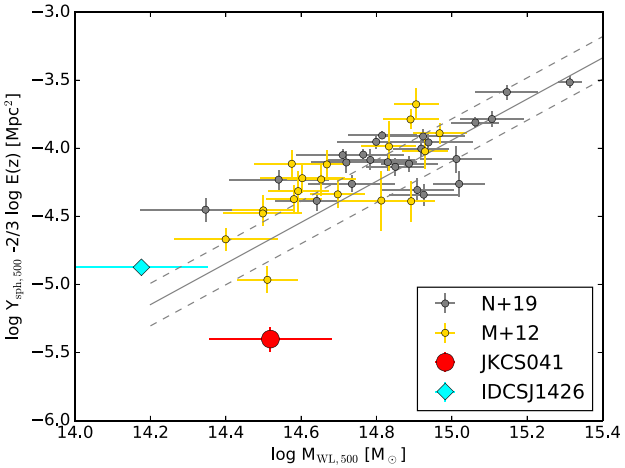

Figure 10. Spherical $Y_{SZ} - M_{WL}$ scaling (aka the SZ mass versus mass plot) for JKCS 041, IDCS J1426.5+3508, and clusters at $z < 0.55$ (from Marrone et al., 2012 and Nagarajan et al., 2019). The solid line indicates the fit to the latter sample while the dashed corridor is the mean model plus and minus the intrinsic scatter (as computed by Nagarajan et al. 2019). JKCS 041 is 0.75 dex below the mean relation, and has a 0.5 dex fainter SZ signal than the lower-mass similar-redshift IDCS J1426.5+3508 cluster, casting doubts on the identification of mass with Y assumed in many past papers.

longer integration time at the same facility (5 versus 28 h). This plot is the common mass-redshift plot except that here we use the observable Y_{SZ} instead of identifying it with mass which removes any ambiguity.

3.2 The SZ mass-mass plot

Fig. 10 shows the spherical Compton Y within r_{500} corrected for the self-similar evolution versus weak lensing mass for JKCS 041, IDCS J1426.5+3508 and the ICM-selected $z < 0.55$ clusters in Marrone et al. (2012) and Nagarajan et al. (2019). JKCS 041 mass is about 0.35 dex larger than the mass of IDCS J1426.5+3508, yet the SZ signal is 0.5 dex lower, i.e. there is a sizeable difference between the mass and the Compton parameter for these two clusters at $z \sim 2$. Some authors might refer to it as a difference between SZ mass and mass. This large difference for just two high redshift clusters alone is enough to cast doubts on the identification of mass with the Compton parameter assumed in many past papers. Indirect evidence of this large scatter is seen in richness versus Y_{SZ} plane, with Y_{SZ} identified with mass, of $z \approx 1$ clusters in Di Mascolo et al. (2020). Under the assumption that the Compton parameter measures mass, Brodwin et al. (2016) concluded that JKCS 041 has a much lower mass than IDCS J1426.5+3508, in spite of its much larger richness of JKCS 041 (Andreon 2013) and of the larger estimate of the weak lensing mass of JKCS 041.

Fig. 10 shows that JKCS 041 is 0.75 dex below the mean mass versus Compton Y relation of the ICM-selected $z < 0.5$ clusters from Nagarajan et al. (2019). The low JKCS 041 Compton parameter for its mass is in line with expectations for merging clusters, observed in simulations to scatter below the mean relation (Wik et al. 2008; Krause et al. 2012). Indeed, according to simulations, merger events cause clusters to scatter downward in this plane because the Y increase is delayed compared the mass growth and because the final Y is lower than that for a cluster of the same final mass (Wik et al. 2008; Krause et al. 2012). According to simulations, the same downscatter would happen to many high redshift clusters, because at early epochs

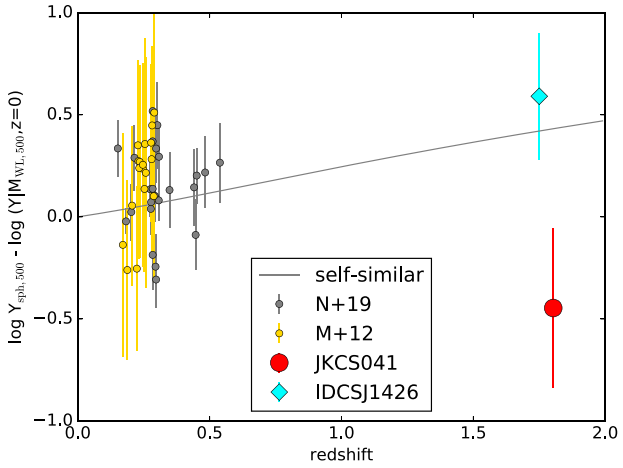

Figure 11. The uncertain evolution of the Compton Y versus mass relation. Distance from the $z = 0$ mean relation of spherical Y_{SZ} versus redshift for JKCS 041, IDCS J1426.5+3508 and clusters at $z < 0.55$ (from Marrone et al. 2012 and Nagarajan et al. 2019). The solid line indicates the $E_z^{2/3}$ self-similar evolution. JKCS 041 is 0.9 dex below it.

the fraction of disturbed or merging clusters is high (Krause et al, 2012). Therefore, we expect a large scatter between SZ mass and true mass at high redshift, with SZ surveys becoming more and more biased against merging cluster as redshift increases. According to simulations, JKCS 041 final equilibrium Y value will be larger by ∼0.2 dex (Wik et al. 2008), insufficient to significantly reduce the SZ mass difference between the two high redshift clusters. As for other comparisons with lower redshift samples (Figs 4, 6, 7, 8, and 9) the relative location of JKCS 041 with respect to the mean relation in Fig. 10) is affected by affected by a hard-to-quantify bias in current low redshift ICM-selected samples.

Fig. 11 shows the same data as previous figure, but with a focus on evolution. The ordinate is the Compton Y distance (at fixed mass) from the $z = 0$ mean relation. The line is the $E_z^{2/3}$ self-similar evolution. Errorbars account for, and are dominated by, mass errors. The figure emphasizes the limited knowledge of evolution of this scaling relation at the cosmic noon due to the dearth of at $z \sim 2$ data. JKCS 041 is 0.9 dex below the self-similar prediction, although with a large error. Also in this plot, the relative JKCS 041 location compared to other samples is partially amplified by a hard-to-quantify bias in current low redshift ICM-selected samples. Furthermore, we note that the observed mass at the cluster redshift is used to estimate the predicted Y using the $z = 0$ relation ignoring mass growth and pseudo-evolution between the two considered redshifts (see Andreon et al. 2021).

3.3 Summary

We present a 28 h long Sunyaev-Zel'dovich (SZ) observation of the $z = 1.803$ JKCS 041 cluster taken with MUSTANG-2 at the Green Bank telescope. This very long exposure allows us to detect JKCS 041, even if the cluster is intrinsically extremely weak compared to other SZ-detected clusters.

We found that the SZ peak is offset from the X-ray centre by about 220 kpc in the direction of the brightest cluster galaxy, which we interpret as due to the cluster being observed just after a major merger, as a part of the emergence of the first massive clusters from the cosmic web at early times.

We found that JKCS 041 has a low central pressure compared to local ICM-selected clusters and a low Compton Y for its mass, likely because the cluster is still in the process of assembly, but also amplified by a hard-to-quantify bias in current low redshift ICM-selected samples. These observations provide us with the measurement of the most distant resolved pressure profile. Comparison with a library of plausibly descendants shows that JKCS 041 pressure profile will likely increase by about 0.7 dex in the next 10 Gyr at all radii.

JKCS 041 has an SZ mass 0.5 dex lower than the lower-mass $z = 1.75$ IDCS J1426.5+3508 cluster, exemplifying at $z \sim 2$ how much different true mass and SZ mass can be.

ACKNOWLEDGEMENTS

SA thanks Sharon Felix, James Jee, Jinhyub Kim, and Lindsay King for useful discussion and for sharing results in advance of publication. The Green Bank Observatory is a facility of the National Science Foundation operated under cooperative agreement by Associated Universities, Inc. MUSTANG-2 data were taken under the project ID AGBT18B-111, AGBT19B-003, AGBT20B-020. CS was supported in part by NASA Chandra grant G01-22120X and XMM grant 80NSSC22K0857.

DATA AVAILABILITY

Raw Chandra data are public available in the Chandra archive, obs ID 15168 and 16321. SZ derived products (beam, transfer function, and map) are available at https://doi.org/10.7910/DVN/AYSGA3.

REFERENCES

Adam R., et al., 2018, A&A, 609, A115
Andreon S., 2013, A&A, 554, A79
Andreon S., 2016, A&A, 587, A158
Andreon S., Maughan B., Trinchieri G., Kurk J., 2009, A&A, 507, 147
Andreon S., Trinchieri G., Pizzolato F., 2011, MNRAS, 412, 2391
Andreon S., Newman A. B., Trinchieri G., Raichoor A., Ellis R. S., Teru T., 2014, A&A, 565, A120
Andreon S., Moretti A., Trinchieri G., Ishwara-Chandra C. H. 2019, A&A, 630, A78
Andreon S., et al., 2021, MNRAS, 505, 5896
Arnaud M., Bohringer H., Jones C. et al., 2009, Astro2020 Decadal Survey (arXiv:0902.4890)
Arnaud M., Pratt G. W., Piffaretti R., Böhringer H., Croston J. H., Pointecouteau E., 2010, A&A, 517, A92
Bocquet S., et al., 2019, ApJ, 878, 55
Bondi M., et al., 2003, A&A, 403, 857
Brodwin M., McDonald M., Gonzalez A. H., Stanford S. A., Eisenhardt P. R., Stern D., Zeimann G. R., 2016, ApJ, 817, 122
Castagna F., Andreon S., 2019, A&A, 632, A22
Castagna F., Andreon S., 2020, A&A, 639, A73
Champagne J. B., et al., 2021, ApJ, 913, 110
Culverhouse T. L., et al., 2010, ApJ, 723, L78
Di Mascolo L., et al., 2019, A&A, 628, A100
Di Mascolo L., et al., 2020, A&A, 638, A70
Di Mascolo L., et al., 2023, Nature, 615, 809
Dicker S. R., et al., 2014, Proc. SPIE, 91530J
Dicker S. R., et al., 2020, ApJ, 902, 144
Diemer B., Joyce M., 2019, ApJ, 871, 168
Dolag K., Komatsu E., Sunyaev R., 2016, MNRAS, 463, 1797
Ebeling H., White D. A., Rangarajan F. V. N., 2006, MNRAS, 368, 65
Fakhouri O., Ma C.-P., Boylan-Kolchin M., 2010, MNRAS, 406, 2267
Felix et al., 2023, in preparation
Fomalont E., et al., 2014, Messenger, 155, 19

Ghirardini V., Ettori S., Amodeo S., Capasso R. Sereno M. 2017, A&A, 604, A100
Ghirardini V., et al., 2019, A&A, 621, A41
Hilton M., et al., 2021, ApJS, 253, 3
Hirschmann M., et al., 2014, MNRAS, 442, 2304
Jee M. J., Ko J., Perlmutter S., Gonzalez A., Brodwin M., Linder E., Eisenhardt P., 2017, ApJ, 847, 117
Kéruzoré F., et al., 2020, A&A, 644, A93
Kim et al., 2023, in preparation
McDonald M., et al., 2014, ApJ, 794, 67
McNamara B. R., Nulsen P. E. J., Wise M. W., Rafferty D. A. Carilli C. Sarazin C. L. Blanton E. L. 2005, Nature, 433, 45
Madau P., Dickinson M., 2014, ARA&A, 52, 415
Mantz A. B., et al., 2018, A&A, 620, A2
Marrone D. P., et al., 2012, ApJ, 754, 119
Massardi M., Ekers R. D., Ellis S. C., Maughan B., 2010, ApJ, 718, L23
Menanteau F., et al., 2012, ApJ, 748, 7
Nagai D., Kravtsov A. V., Vikhlinin A., 2007, ApJ, 668, 1
Navarro J. F., Frenk C. S., White S. D. M., 1997, ApJ, 490, 493
Newman A. B., Ellis R. S., Andreon S., Treu T., Raichoor A., Trinchieri G., 2014, ApJ, 788, 51
Planck Collaboration, 2016, A&A, 594, A27
Pratt G. W., Arnaud M., Maughan B. J., Melin J. -B., 2022, A&A, 665, A24
Prichard L. J., et al., 2017, ApJ, 850, 203
Ragagnin A., Dolag K., Biffi V., Cadolle Bel M., Hammer N. J., Krukau A., Petkova M., Steinborn D., 2017, Astron. Comput., 20, 52
Ragagnin A., Saro A., Singh P., Dolag K., 2021, MNRAS, 500, 5056
Ricci M., et al., 2020, A&A, 642, A126
Romero C., et al., 2018, A&A, 612, A39
Romero C. E., et al., 2020, ApJ, 891, 90
Sayers J., et al., 2013, ApJ, 778, 52
Scharf C., 2002, ApJ, 572, 157
Schulz B., Marton G., Valtchanov I. et al., 2017, preprint (arXiv:1706.00448)
Smith R. K., Brickhouse N. S., Liedahl D. A., Raymond J. C., 2001, ApJ, 556, L91
Sunyaev R. A., Zel'dovich Y. B., 1972, A&A, 20, 189
Tozzi P., et al., 2022, A&A, 667, A134
van Kempen T., Kneissl R., Marcelino N. et al., 2014, ALMA Memo, 598
Voit G. M., Balogh M. L., Bower R. G., Bower R. G. Lacey C. G. Bryan G. L. 2003, ApJ, 593, 272
Wik D. R., Sarazin C. L., Ricker P. M., Randall S. W. 2008, ApJ, 680, 17
Willis J. P., et al., 2020, Nature, 577, 39
Zavala J. A., et al., 2021, ApJ, 909, 165
Zhang C., Yu Q., Lu Y., 2014, ApJ, 796, 138.

This paper has been typeset from a TEX/LATEX file prepared by the author.

List of astronomical key words (Updated on 2020 January)

This list is common to *Monthly Notices of the Royal Astronomical Society, Astronomy and Astrophysics*, and *The Astrophysical Journal*. In order to ease the search, the key words are subdivided into broad categories. No more than *six* subcategories altogether should be listed for a paper.

The subcategories in boldface containing the word 'individual' are intended for use with specific astronomical objects; these should never be used alone, but always in combination with the most common names for the astronomical objects in question. Note that each object counts as one subcategory within the allowed limit of six.

The parts of the key words in italics are for reference only and should be omitted when the keywords are entered on the manuscript.

General
editorials, notices
errata, addenda
extraterrestrial intelligence
history and philosophy of astronomy
miscellaneous
obituaries, biographies
publications, bibliography
sociology of astronomy
standards

Physical data and processes
acceleration of particles
accretion, accretion discs
asteroseismology
astrobiology
astrochemistry
astroparticle physics
atomic data
atomic processes
black hole physics
chaos
conduction
convection
dense matter
diffusion
dynamo
elementary particles
equation of state
gravitation
gravitational lensing: micro
gravitational lensing: strong
gravitational lensing: weak
gravitational waves
hydrodynamics
instabilities
line: formation
line: identification
line: profiles
magnetic fields
magnetic reconnection
(magnetohydrodynamics) MHD
masers
molecular data
molecular processes
neutrinos
nuclear reactions, nucleosynthesis, abundances
opacity
plasmas
polarization
radiation: dynamics
radiation mechanisms:general
radiation mechanisms: non-thermal
radiation mechanisms: thermal
radiative transfer
relativistic processes
scattering
shock waves
solid state: refractory
solid state: volatile
turbulence
waves

Astronomical instrumentation, methods and techniques
atmospheric effects
balloons
instrumentation: adaptive optics
instrumentation: detectors
instrumentation: high angular resolution
instrumentation: interferometers
instrumentation: miscellaneous
instrumentation: photometers
instrumentation: polarimeters
instrumentation: spectrographs
light pollution
methods: analytical
methods: data analysis
methods: laboratory: atomic
methods: laboratory: molecular
methods: laboratory: solid state
methods: miscellaneous
methods: numerical
methods: observational
methods: statistical
site testing
space vehicles
space vehicles: instruments
techniques: high angular resolution
techniques: image processing
techniques: imaging spectroscopy
techniques: interferometric
techniques: miscellaneous
techniques: photometric
techniques: polarimetric
techniques: radar astronomy
techniques: radial velocities
techniques: spectroscopic
telescopes

Astronomical data bases
astronomical data bases: miscellaneous
atlases
catalogues
surveys
virtual observatory tools

Software
software: data analysis
software: development
software: documentation
software: public release
software: simulations

Astrometry and celestial mechanics
astrometry
celestial mechanics
eclipses
ephemerides
occultations
parallaxes
proper motions
reference systems
time

The Sun
Sun: abundances
Sun: activity
Sun: atmosphere
Sun: chromosphere
Sun: corona
Sun: coronal mass ejections (CMEs)
Sun: evolution
Sun: faculae, plages
Sun: filaments, prominences
Sun: flares
Sun: fundamental parameters
Sun: general
Sun: granulation
Sun: helioseismology
Sun: heliosphere
Sun: infrared
Sun: interior
Sun: magnetic fields
Sun: oscillations
Sun: particle emission
Sun: photosphere
Sun: radio radiation
Sun: rotation
(Sun:) solar–terrestrial relations
(Sun:) solar wind
(Sun:) sunspots
Sun: transition region
Sun: UV radiation
Sun: X-rays, gamma-rays

Planetary systems
comets: general

comets: individual: . . .
Earth
interplanetary medium
Kuiper belt: general

Kuiper belt objects: individual: . . .
meteorites, meteors, meteoroids
minor planets, asteroids: general
minor planets, asteroids: individual: . . .
Moon
Oort Cloud
planets and satellites: atmospheres
planets and satellites: aurorae
planets and satellites: composition
planets and satellites: detection
planets and satellites: dynamical evolution and stability
planets and satellites: formation
planets and satellites: fundamental parameters
planets and satellites: gaseous planets
planets and satellites: general

planets and satellites: individual: . . .
planets and satellites: interiors
planets and satellites: magnetic fields
planets and satellites: oceans
planets and satellites: physical evolution
planets and satellites: rings
planets and satellites: surfaces
planets and satellites: tectonics
planets and satellites: terrestrial planets
planet–disc interactions
planet–star interactions
protoplanetary discs
zodiacal dust

Stars
stars: abundances
stars: activity
stars: AGB and post-AGB
stars: atmospheres
(stars:) binaries *(including multiple)*: close
(stars:) binaries: eclipsing
(stars:) binaries: general
(stars:) binaries: spectroscopic
(stars:) binaries: symbiotic
(stars:) binaries: visual
stars: black holes
(stars:) blue stragglers
(stars:) brown dwarfs
stars: carbon
stars: chemically peculiar
stars: chromospheres
(stars:) circumstellar matter
stars: coronae
stars: distances
stars: dwarf novae
stars: early-type
stars: emission-line, Be
stars: evolution
stars: flare
stars: formation
stars: fundamental parameters
(stars:) gamma-ray burst: general
(stars:) **gamma-ray burst: individual: . . .**
stars: general
(stars:) Hertzsprung–Russell and colour–magnitude diagrams
stars: horizontal branch
stars: imaging
stars: individual: . . .
stars: interiors

stars: jets
stars: kinematics and dynamics
stars: late-type
stars: low-mass
stars: luminosity function, mass function
stars: magnetars
stars: magnetic fields
stars: massive
stars: mass-loss
stars: neutron
(stars:) novae, cataclysmic variables
stars: oscillations *(including pulsations)*
stars: peculiar *(except chemically peculiar)*
(stars:) planetary systems
stars: Population II
stars: Population III
stars: pre-main-sequence
stars: protostars
(stars:) pulsars: general
(stars:) **pulsars: individual: . . .**
stars: rotation
stars: solar-type
(stars:) starspots
stars: statistics
(stars:) subdwarfs
(stars:) supergiants
(stars:) supernovae: general
(stars:) **supernovae: individual: . . .**
stars: variables: Cepheids
stars: variables: Scuti
stars: variables: general
stars: variables: RR Lyrae
stars: variables: S Doradus
stars: variables: T Tauri, Herbig Ae/Be
(stars:) white dwarfs
stars: winds, outflows
stars: Wolf–Rayet

Interstellar medium (ISM), nebulae
ISM: abundances
ISM: atoms
ISM: bubbles
ISM: clouds
(ISM:) cosmic rays
(ISM:) dust, extinction
ISM: evolution
ISM: general
(ISM:) HII regions
(ISM:) Herbig–Haro objects

ISM: individual objects: . . .
(except planetary nebulae)
ISM: jets and outflows
ISM: kinematics and dynamics
ISM: lines and bands
ISM: magnetic fields
ISM: molecules
(ISM:) photodissociation region (PDR)
(ISM:) planetary nebulae: general
(ISM:) **planetary nebulae: individual: . . .**
ISM: structure
ISM: supernova remnants

The Galaxy
Galaxy: abundances
Galaxy: bulge
Galaxy: centre
Galaxy: disc
Galaxy: evolution
Galaxy: formation
Galaxy: fundamental parameters
Galaxy: general
(Galaxy:) globular clusters: general
(Galaxy:) **globular clusters: individual: . . .**
Galaxy: halo
Galaxy: kinematics and dynamics
(Galaxy:) local interstellar matter
Galaxy: nucleus
(Galaxy:) open clusters and associations: general
(Galaxy:) **open clusters and associations: individual: . . .**
(Galaxy:) solar neighbourhood
Galaxy: stellar content
Galaxy: structure

Galaxies
galaxies: abundances
galaxies: active
galaxies: bar
(galaxies:) BL Lacertae objects: general
(galaxies:) **BL Lacertae objects: individual: . . .**
galaxies: bulges
galaxies: clusters: general

galaxies: clusters: individual: . . .
galaxies: clusters: intracluster medium
galaxies: disc
galaxies: distances and redshifts
galaxies: dwarf
galaxies: elliptical and lenticular, cD
galaxies: evolution
galaxies: formation
galaxies: fundamental parameters
galaxies: general
galaxies: groups: general

galaxies: groups: individual: . . .
galaxies: haloes
galaxies: high-redshift

galaxies: individual: . . .
galaxies: interactions
(galaxies:) intergalactic medium
galaxies: irregular
galaxies: ISM
galaxies: jets
galaxies: kinematics and dynamics
(galaxies:) Local Group
galaxies: luminosity function, mass function
(galaxies:) Magellanic Clouds
galaxies: magnetic fields
galaxies: nuclei
galaxies: peculiar
galaxies: photometry
(galaxies:) quasars: absorption lines
(galaxies:) quasars: emission lines
(galaxies:) quasars: general

(galaxies:) **quasars: individual: . . .**
(galaxies:) quasars: supermassive black holes
galaxies: Seyfert
galaxies: spiral
galaxies: starburst
galaxies: star clusters: general

galaxies: star clusters: individual: . . .
galaxies: star formation
galaxies: statistics
galaxies: stellar content
galaxies: structure

Cosmology
(cosmology:) cosmic background radiation
(cosmology:) cosmological parameters
(cosmology:) dark ages, reionization, first stars
(cosmology:) dark energy
(cosmology:) dark matter
(cosmology:) diffuse radiation
(cosmology:) distance scale
(cosmology:) early Universe
(cosmology:) inflation
(cosmology:) large-scale structure of Universe
cosmology: miscellaneous
cosmology: observations
(cosmology:) primordial nucleosynthesis
cosmology: theory

Resolved and unresolved sources as a function of wavelength
gamma-rays: diffuse background
gamma-rays: galaxies
gamma-rays: galaxies: clusters
gamma-rays: general
gamma-rays: ISM
gamma-rays: stars
infrared: diffuse background
infrared: galaxies
infrared: general
infrared: ISM
infrared: planetary systems
infrared: stars
radio continuum: galaxies
radio continuum: general
radio continuum: ISM
radio continuum: planetary systems
radio continuum: stars
radio continuum: transients
radio lines: galaxies
radio lines: general
radio lines: ISM
radio lines: planetary systems
radio lines: stars
submillimetre: diffuse background
submillimetre: galaxies
submillimetre: general
submillimetre: ISM
submillimetre: planetary systems
submillimetre: stars
ultraviolet: galaxies
ultraviolet: general
ultraviolet: ISM
ultraviolet: planetary systems
ultraviolet: stars
X-rays: binaries
X-rays: bursts
X-rays: diffuse background
X-rays: galaxies
X-rays: galaxies: clusters
X-rays: general
X-rays: individual: . . .
X-rays: ISM
X-rays: stars

Transients
(transients:) black hole mergers
(transients:) black hole - neutron star mergers
(transients:) fast radio bursts
(transients:) gamma-ray bursts
(transients:) neutron star mergers
transients: novae
transients: supernovae
transients: tidal disruption events